NeuroImage: Clinical 5 (2014) 332–340

Contents lists available at ScienceDirect

NeuroImage: Clinical

journal homepage: www.elsevier.com/locate/ynicl

Using longitudinal metamorphosis to examine ischemic stroke lesion dynamics on perfusion-weighted images and in relation to final outcome on T2-w images

Islem Rekik[a,b,*], Stéphanie Allassonnière[b], Trevor K. Carpenter[a], Joanna M. Wardlaw[a]

[a] Division of Neuroimaging Sciences, Brain Research Imaging Centre, University of Edinburgh, UK
[b] CMAP, Ecole Polytechnique, Route de Saclay, 91128 Palaiseau, France

ARTICLE INFO

Article history:
Received 22 April 2014
Received in revised form 25 June 2014
Accepted 21 July 2014
Available online 1 August 2014

Keywords:
Longitudinal metamorphosis
Acute/subacute ischemic stroke
Dynamic evolution
Perfusion

ABSTRACT

We extend the image-to-image metamorphosis into constrained longitudinal metamorphosis. We apply it to estimate an evolution scenario, in patients with acute ischemic stroke, of both scattered and solitary ischemic lesions visible on serial MR perfusion weighted imaging from acute to subacute stages. We then estimate a patient-specific residual map that enables us to capture the most relevant shape and intensity changes, continuously, as the lesion evolves from acute through subacute to chronic timepoints until merging into the final image. We detect areas with high residuals (i.e., high dynamics) and identify areas that became part of the final T2-w lesion obtained at ≥1 month after stroke. This allows the investigation of the dynamic influence of perfusion values on the final lesion outcome as seen on T2-w imaging. The model provides detailed insights into stroke lesion dynamic evolution in space and time that will help identify factors that determine final outcome and identify targets for interventions to improve outcome.

1. Introduction

Stroke is the third leading cause of death in industrialized countries and a major cause of death worldwide. Ischemia – the commonest type of stroke – results from disruption of blood flow within the brain caused by occlusion of an artery. Efforts to improve the treatment of ischemic stroke target 'brain tissue at risk of infarction' (the penumbra) that can revert to a normal state following successful recanalization of the occluded artery within the first few hours after onset (Wardlaw, 2010). Multi-modality brain imaging is widely used in acute stroke management for diagnosis, prognosis and treatment planning. In particular, diffusion-weighted imaging (DWI) and perfusion-weighted imaging (PWI) are frequently used to detect early ischemic changes and distinguish between permanently damaged and salvageable tissues. However, while medical imaging has improved our understanding of stroke for the last decades, it is still not possible to determine the 'best' treatment in any one individual patient (Wardlaw et al., 2012). One reason for that is the wide spectrum of stroke lesion patterns and the lack of understanding of factors governing lesion evolution. Particularly, stroke lesions are frequently multicomponent, appear and disappear, distort adjacent tissues and have ill-defined boundaries (Rekik et al., 2012). A second reason is the wide use of basic volumetric analysis and thresholding tools for assessing a stroke lesion and selecting patients for clinical trials (Davis et al., 2008; Furlan et al., 2006; Hacke et al., 2005). These basic quantitative techniques fundamentally limit our scope for examining stroke dynamics as they do not capture the direction, locality or the speed of stroke lesion evolution.

This suggests the need for better methods to overcome the limitations of these techniques and accurately characterize stroke lesion dynamics. As highlighted in the review paper (Rekik et al., 2012), no patient-specific dynamic models had been developed to map in detail the kinetics of the lesion evolution and to estimate the spatiotemporal deformations that ischemic tissue undergoes. Recent work by (Rekik et al., 2013) began the exploration of advanced spatiotemporal (4D) models for studying the dynamics of stroke evolution in longitudinal data. The applied current deformation model enabled the identification of areas of contraction and expansion in stroke lesion surfaces, which allowed us to investigate correlations between perfusion and diffusion lesion surface evolutions (Rekik et al., 2013). Although this model proved to be a mathematically robust representation of the lesion surface, it could not incorporate image intensity measures in its abstract mathematical framework. Hence, there was no possibility of using this model to study the effects of DWI or PWI or other tissue parameter values on lesion dynamics. Furthermore, it was not suitable for lesions

* Corresponding author at: Department of Neuroimaging Sciences, Centre for Clinical Brain Sciences, The University of Edinburgh, Chancellor's Building, 49 Little France Crescent, Edinburgh EH16 4SB, UK.
E-mail addresses: islem.rekik@gmail.com (I. Rekik), stephanie.allassonniere@polytechnique.edu (S. Allassonnière), trevor.carpenter@ed.ac.uk (T.K. Carpenter), joanna.wardlaw@ed.ac.uk (J.M. Wardlaw).

http://dx.doi.org/10.1016/j.nicl.2014.07.009

where the number of components varied with time. However, scattered multicomponent lesions and variable patterns of perfusion and diffusion abnormality progression are very common (84% of our cohort) (Ogata et al., 2011).

To partly overcome these limitations, we used a more versatile approach, the metamorphosis model — introduced by Trouvé and Younes (2005), which handles both multi-component and solitary lesions and incorporates gray-scale intensities into the 3D image evolution. To examine the influence of perfusion values on final tissue outcome, we extend the work presented in Garcin and Younes (2005) from two-image based metamorphosis to time-series based *longitudinal metamorphosis* and introduce a new constraint on the velocity path to force its regularity in time. We identified one recent paper that addressed longitudinal image evolution using metamorphosis. Hong et al. (2012) adapted the work of Niethammer et al. (2011) by proposing a metamorphic geodesic regression using appropriate averaging of independent pairwise metamorphoses. In this paper, we present a different and more compact formulation for longitudinal metamorphosis using an ordered set $\mathfrak{I} = \{I_0, I_1, \ldots, I_N\}$ of N images. Unlike Hong et al. (2012), our approach does not require a pairwise estimation of $N + 1$ metamorphoses using geodesic regression. Instead, the method estimates a single metamorphosis that exactly meets all the intermediate images (observations) in $\mathfrak{I}$, while enforcing regularity in time for the estimated velocity field (Fig. 1).

The remainder of this paper is structured as follows. In Section 2, we will describe the image-to-image formulation of the metamorphosis theory and its extension to longitudinal data. In Section 3, we present the results of *longitudinal metamorphosis* to both synthetic images and perfusion ischemic lesion and investigate the relation of the metamorphic residual to the final T2-w lesion boundary. Finally, we present a critical overall analysis, presenting the major findings and limitations of our model and revealing new avenues for exploration in ischemic stroke.

2. Methods

2.1. Image-to-image metamorphosis

2.1.1. Prior to the metamorphosis era: the diffeomorphic era

The serial medical imaging and the increasingly acquired datasets to study changes in anatomy and brain disease evolution have triggered the development of compelling mathematical frameworks based on deformations (Klein et al., 2009). A specific category of spatial deformations has spanned the attention of researchers in this field: diffeomorphisms (smooth deformation with a smooth inverse). These were largely used in different registration models (Allassonnière et al., 2005; Beg et al., 2005; Holland and Dale, 2011; Klein et al., 2009) and became a part of the classical deformable template theory – especially after the establishment of the Large Deformation Diffeomorphic Metric Mapping (LDDMM) – pioneered by Dupuis et al. (1998) and Trouvé (1995, 1998). The metamorphosis theory is built upon the LDDMM framework which is based on the idea of a diffeomorphic metric. This metric is a distance on the object space – seen as a Riemannian manifold – which results from the transportation of a metric on the group of diffeomorphisms by a group action. This defines a distance between two objects through the geodesic diffeomorphic path which connects one to the other. In the following, we will only consider *objects* which are *images*. The estimated diffeomorphic transformation g_1 connects a source image I_0 to a target image I_1 as follows: $I_0 \circ g_1^{-1} = I_1$. The central idea of LDDMM is that g_1 is the mapping at time 1 of a deformation path. What drives the evolution of this transformation from g_0 to g_1 is the flow equation: given $v_t(g(t))$ a velocity vector field

$$\begin{cases} \dfrac{dg(t)}{dt} = v_t(g(t)) \\ g_0 = id \end{cases} \tag{1}$$

where id is the identity map.

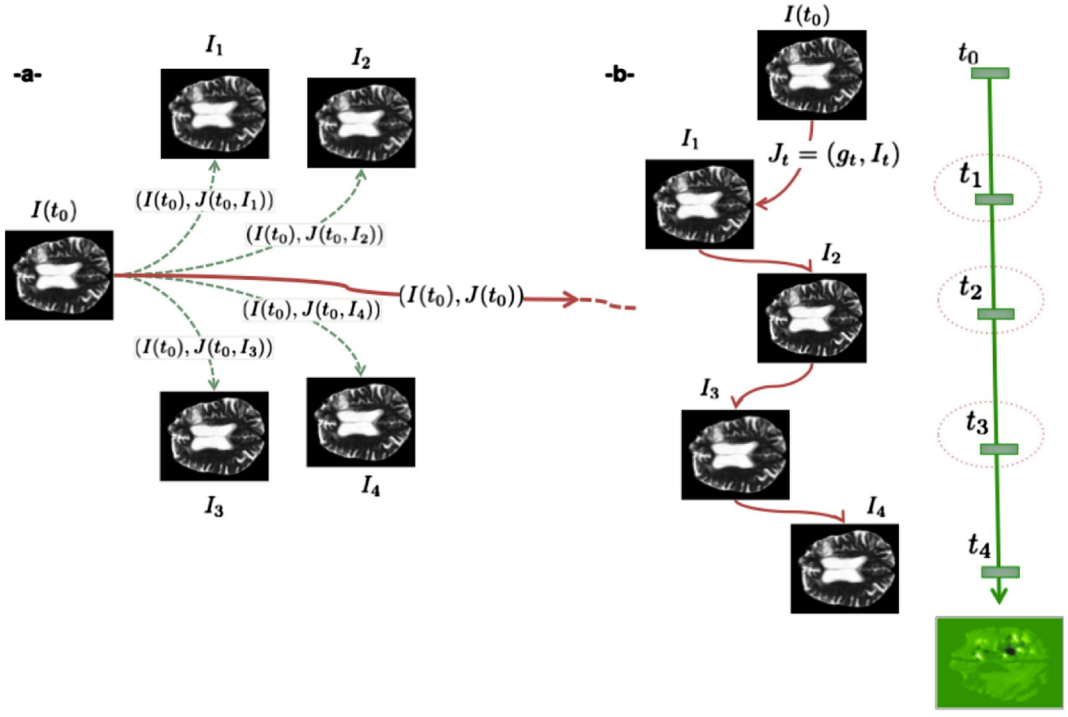

Fig. 1. Comparison between metamorphic regression scheme presented in Hong et al. (2012) (a) and our longitudinal metamorphosis (b). The red bold line in (a) represents the metamorphic regression line determined by pairwise metamorphoses between the baseline image $I(t_0)$ and the images I_i. Each individual metamorphosis is defined by the initial momentum of the geodesic shooting. In (b), the estimated longitudinal metamorphosis path J_t morphs the baseline image successively into I_1, I_2, and I_3 till merging with the final image I_4. To avoid the velocity jumps we force the estimated velocity to be continuous in time at the observation timepoints $\{t_0, t_1, \ldots\}$.

However, a major shortcoming of the *diffeomorphic* metric is that it does not allow variations in the topology of the deformed object. For this reason, it is commonly used to study changes in anatomical structures (as connected sets remain connected and disjoint sets remain disjoint) rather than in brain lesions that may take dissimilar forms and undergo a topology change (such as the appearance of new disconnected sets of ischemic regions in stroke or the merging of different sets into a bigger one). To overcome this shortcoming, a different mathematical formulation introduced a slight modification in the idea of the diffeomorphic metric (Trouvé and Younes, 2005). This led to the definition of a new metric: the metamorphic metric.

2.1.2. The metamorphosis theory

Proposed by Trouvé and Younes (2005), metamorphosis is an efficient non-linear registration method that aligns two images by jointly estimating an optimal velocity deformation vector field v_t and an optimal intensity scalar field I_t. The idea of metamorphosis stems from including the infinitesimal variation of the gray level of the image in the metric used to estimate the geodesics of deformations accounting for intensity change and producing the *metamorphic metric*. The definition of this metric requires the use of appropriate spaces to which images, forces acting on them, and velocities driving the evolutions of the baseline image towards the target images belong. The mathematical framework for metamorphosis is composed of the three main components:

- *Image*: an image I is an element of the square integrable set of functions $M = L^2(\Omega)$ considered as a Riemannian manifold (the object space) with Ω as the support of I. A curve $(t \mapsto I_t, t \in [0, 1])$ on M is the evolution path of a base line image I_0. M is equipped with the usual metric on L^2.
- *Action (force)*: an action $g \in G$ is a diffeomorphic transformation which acts upon the object space M. In the realm of a classical diffeomorphic deformation theory, the action g is associated to the velocity v through the flow equation (Eq. (1)). A curve $(t \mapsto g_t, t \in [0, 1])$ on G acting on $I \in M$ describes a path of deformation morphing I over the time interval [0, 1].
- *Velocity*: for all $t \in [0, 1]$, the velocity field v_t belongs to the vector space V, which is the tangent space to the action group G. We adopt a similar construction as in that of Beg et al. (2005) for the velocity vector space V on which smoothness constraints are placed to ensure the existence of optimal smooth solutions in the space of diffeomorphisms for the flow equation (Eq. (1)). We endowed the velocity vector space V with an inner product $<.,.>_V$ defined through a differential Cauchy–Navier type operator L (with adjoint $L^\dagger$) given by: $<f, g>_V = <Lf, Lg>_{L^2} = <L^\dagger Lf, g>_{L^2}$ where $<.,.>_{L^2}$ is the standard L^2 inner-product for square integrable vector fields on M and the Cauchy–Navier differential operator as presented in Beg et al. (2005) $L = (-\alpha\nabla^2 + \gamma)I_d$ (I_d is the identity matrix). Thus, the required smoothness of the deformations is specified by the norm of the space V of smooth velocity vector fields through L.

As defined by Trouvé and Younes (2005), a metamorphosis is a pair of curves $((g(t), I(t)), t \in [0, 1])$ on the product space $\mathscr{M} = G \times M$, with $g(0) = id$. The effective metamorphosis path $J(t)$ on M is defined as a combination of the action deformation path $g(t)$ and the image path $I(t)$ which is the residual of the deformation on M: $J(t) = g(t) \cdot I(t)$. All details of metamorphosis are available in Trouvé and Younes (2005).

As shown in Garcin and Younes (2005), the optimal metamorphosis curves $((g(t), I(t)), t \in [0, 1])$ – morphing the source image I_0 into target one I_1 – are estimated by minimizing the cost functional $U(I, v)$:

$$U(I,v) = \int_0^1 |v|_V^2 dt + \frac{1}{\sigma^2}\int_0^1 \left|\frac{dI(t)}{dt} + \nabla I_t \cdot v_t\right|_{L^2}^2 dt. \quad (2)$$

The term $\nabla I_t \cdot v_t$ represents the spatial variation of the moving image I_t in the direction v_t. Furthermore, the moving intensity scalar field I_t is defined under the action of the diffeomorphism g_t on a baseline image $I_0 : I_t = g_t \cdot I_0$. This nicely brings us to the diffeomorphic flow equation (Eq. (1)) that is driven by a sufficiently smooth deformation vector field to estimate (Beg et al., 2005; Trouvé, 1998). All the previous equations have the fundamental property to remain geodesic equations in the image manifold M. Their solution is sought through a minimization algorithm, which provides an efficient and robust estimation of intensity variation and diffeomorphisms — in case of large deformations (Trouvé and Younes, 2005).

This formulation unifies a common mathematical framework intensity change and deformation. The residual of the deformation term $|\delta(t)|^2_{I(t)} = |\frac{dI(t)}{dt} + \nabla I_t \cdot v_t|^2_{L^2}$ undertakes that the metamorphosis scheme includes the variations in the image evolution path $I(t)$ induced by the deformation field v_t, thereby it can be viewed as a condensed form that sums up both variations in intensity and shape.

As we need to minimize this energy for image matching, a discretization step in the time and space domains is required. We reproduce the discretization scheme proposed by Garcin and Younes (2005) for the image-to-image metamorphosis where we approximate the term $\nabla I_t \cdot v_t$ by $(I(t+1, x + v(t,x)) - I(t,x))$ as follows:

$$\lim_{\epsilon \to 0} \frac{I(t+\epsilon, x+\epsilon v(t,x)) - I(t,x)}{\epsilon} = \frac{\partial I(t,x)}{dt} + \frac{\partial I(t,x)}{dx} \cdot v(t,x). \quad (3)$$

Next, we discretize the energy functional in the discrete time domain of evolution $[0, T]$ (with the size of a timestep Δt being such that $T = n \times \Delta t$) and in the image space domain (a grid). We use a trilinear interpolation proposed by Garcin and Younes (2005) to define real values for $x + v_t(x)$:

$$\Gamma_{v_t} I_{t+1} : x \in \Omega \to \Gamma(I_{t+1})(x + v_t(x)) = I(t+1, x + v(t,x)) \in \mathbb{R}.$$

By applying the trilinear operator Γ to $I_{t+1}(x + v_t(x))$, we get:

$$\begin{cases} U(I,v) = \sum_{t=0}^{T-1} |v_t|_V^2 + \frac{1}{\sigma^2} \sum_{t=0}^{T-1} \sum_{x \in \Omega} |\Gamma(I_{t+1})(x + v_t(x)) + \nabla I_t \cdot v_t|_{L^2}^2 \\ v_{t_0} = v_{t_1} \text{ and } v_{T-1} = v_T \end{cases} \quad (4)$$

We initialize the image evolution path from the source I_0 to the target image I_1 through piece-wise trilinear interpolation (fixed boundary conditions for exact matching): $I(t) = (1-t)I_0 + tI_1$; with $t \in [0, T]$. Ultimately, the minimal metamorphosis path composed of both the o ptimal image path $(t \mapsto I_t, t \in [0, 1])$ and the associated diffeomorphic path $(t \mapsto g_t, t \in [0, 1])$ is calculated using the metamorphosis energy gradients $(\nabla_{I_t} U, \nabla_{v_t} U)$ in a standard alternating steepest gradient descent algorithm:

$$\nabla_{I_t} U(I,v) = \frac{2}{\sigma^2} I_t - \Gamma_{v_t} I_{t+1} + \Gamma^T_{v_{t-1}} \left(\Gamma_{v_{t-1}} I_t - I_{t-1}\right) \quad (5)$$

$$\nabla_{v_t} U(I,v) = 2v_t + \frac{2}{\sigma^2}\left[\left(\Gamma_{v_t} \nabla_x I_{t+1}\right)^T \left(\Gamma_{v_t} I_{t+1} - I_t\right)\right]. \quad (6)$$

2.2. Constrained longitudinal metamorphosis using N images

Now we will present the generalization to a set of time dependent observations. We aim to estimate a metamorphosis (w.r.t. the metamorphosis metric) for which we constrain the velocity vector field $(v_t)_{t \in [0,1]}$ to be continuous in time in particular at the observation timepoints. This is based on similar equations as before and the energy to minimize becomes:

$$\begin{cases} U(I,v) = \sum_{t=0}^{T-1} |v_t|_V^2 + \frac{1}{\sigma^2} \sum_{t=0}^{T-1} \sum_{x \in \Omega} |\Gamma(I_{t+1})(x + v_t(x)) + \nabla I_t \cdot v_t|_{L^2}^2 \\ v_{t_0} = v_{t_1} \quad v_{T-1} = v_T \text{ and } v_{t-1} = v_t = v_{t+1} \text{ for } t \in \{1, \ldots, T-1\} \end{cases} \quad (7)$$

where $(v_t)_{t\in[0,1]}$ is continuous in time. We enforce the continuity of the velocity vector field so that the whole path is continuous in time. This is done as follows: for any observation timepoint $t = t_{obs}$:

$$v_{t_{obs}} = v^{+}_{t_{obs}} = v^{-}_{t_{obs}}. \quad (8)$$

We choose a small time discretization step between the observations for this definition of regularity in time to be valid. This constraint forces the estimated metamorphosis to follow a relevant path (w.r.t. our application) and makes it differ from concatenated paths as illustrated in Fig. 2.

In order to minimize this energy and get the longitudinal metamorphosis using N images $\mathfrak{I} = \{I_0, I_1, \ldots, I_N\}$, we exactly follow the steps of the gradient descent pipeline using Eqs. (5)–(6), except that we modify two steps. In the first step, we initialize image evolution path from the source image I_0 to the target image I_N through piece-wise trilinear interpolation (fixed boundary conditions for exact matching). However, we force the algorithm to exactly go through all observations (time-series images) by keeping the observations unaltered and only updating the intensity path connecting them. The second change is that we impose a time-continuity constraint on the estimated velocity which forces relevant final deformation maps in a way that would better capture the dynamics of the lesions.

3. Material

3.1. Patient recruitment [10 patients]

We test the metamorphosis model on 10 representative patients from a study of serial MR imaging in hyperacute stroke, representing a range of stroke severity (mean ± std dev.): (NIHSS = 12.6 ± 8.9), age (74 ± 9.47 years) and acute mean transit time (MTT) volume ($1.78 \pm 1.23 \cdot 10^5$ mm^3). We include patients who had PWI images at around 5 h, the second at around 5 ± 1 days and the third at 10.5 ± 2.5 days after stroke and T2-weighted image lesion at ≥ month after stroke. Furthermore, we have checked that swelling in the recruited patients did not distort DWI lesion boundary as it can mislead the result interpretations.

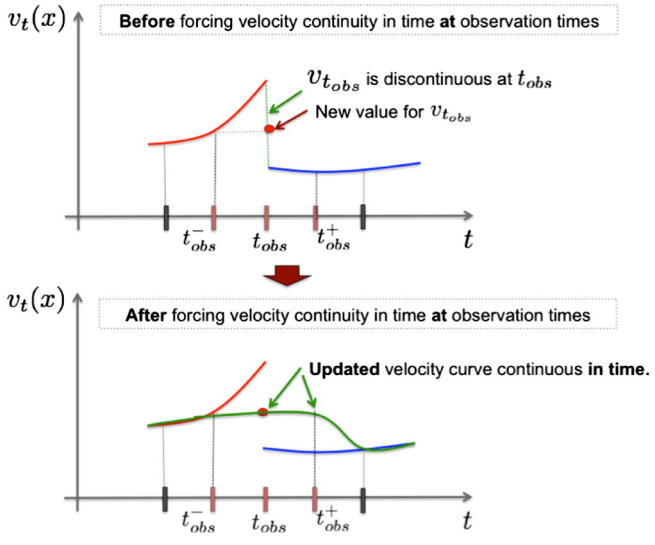

Fig. 2. Enforcing the continuity in time of the estimated velocity field (v_t) at observation timepoints. (Top) For a fixed voxel x in the image, we notice that the velocity curve v_t is discontinuous at observation timepoints t_{obs} as both the red and blue curves are not "glued" together. We enforce the continuity at the observation timepoints by associating a new value to v_{obs} at t_{obs} that is equal to the velocity value at t^-_{obs} then we update t^+_{obs} to establish the equality between the three discrete points in time. This generates a new velocity curve (in green) that is continuous in time.

3.2. MR imaging and pre-processing steps

All MR images were acquired using a GE Sigma LX 1.5-T MR scanner (General Electric, Milwaukee, Wisconsin) with a birdcage quadrature coil and a standardized protocol for acute stroke. The spin-echo echoplanar imaging diffusion tensor axial sequences and dynamic susceptibility contrast echoplanar imaging PWI had 15 axial slices each of 6 mm thickness with an interslice gap of 0.97 mm and an imaging matrix of 128 × 128 encompassing a 240 × 240 mm field of view. MTT perfusion maps were generated using PWI data, full details of the image acquisition and processing protocol have been described previously in Rivers et al. (2007). The MTT and final follow-up T2-weighted images (at ≥1 month after stroke) were co-registered using a 3D affine transformation and their corresponding visible lesions were manually delineated on every slice by an expert. Similarly the perfusion series were registered to the diffusion series (Bastin and Armitage, 2000). We used affine registration to compensate for these effects and account for patient motion, similar procedures have been applied elsewhere (Huang et al., 2008). Normalized mutual information was used as a similarity measure since the contrast between the diffusion baseline image and other images is dependent upon the direction of diffusion weighting — likewise the perfusion series before and after the arrival of gadolinium contrast.

4. Results

4.1. Comparison between the proposed longitudinal metamorphosis and independent metamorphoses

In this section, we compare the synthetic results of our method with respect to those of a modest concatenation of individual metamorphoses. Note that this concatenation does not make any assumption on the continuity of the deformation field so that it will most probably be discontinuous at the observation timepoints. This problem should be avoided by our method and therefore better fit the real behavior of the lesion. To perform this, we introduce a synthetic example where the comparison is easier and preliminary observations are made.

We have tested the proposed longitudinal metamorphosis which is the solution of an energy minimization under constraint on synthetic images (two small spheres merging into one sphere then expanding into a bigger one, Fig. 3). Our approach is different from the estimation of successive independent metamorphoses from image at t_1 to image at t_2 then from image at t_2 to image at t_3, etc., then gluing these bits all together to build the longitudinal metamorphosis scenario. More importantly, we show in Fig. 3 successive snapshots of the estimated velocity field magnitude for the proposed *constrained longitudinal metamorphosis* that goes through three synthetic images (Fig. 3-B, first row) and for an image-to-image metamorphosis concatenating two independent metamorphoses (one morphing image 1 into image 2 and a second one morphing image 2 into image 3) (Fig. 3-B, second row). The visual comparison of both evolution scenarios shows a lack of a transition phase between metamorphosis I and metamorphosis II: the concatenation process of two independent metamorphoses create an abrupt change in the estimated velocity field. However, the constrained longitudinal metamorphosis includes an in-between transition phase between the pairs of evolution {image 1 → image 2} and {image 2 → image 3} at the observation timepoint t_2 (outlined in red in Fig. 3). Therefore the evolution of the set of synthetic images seems more *natural* in the first estimated longitudinal metamorphosis scenario.

4.2. Metamorphic longitudinal matching applied to perfusion MR images of stroke

For every patient, we estimated a longitudinal metamorphosis of MTT lesion from acquisition timepoints t_1 to t_3. Both velocity and intensity paths are presented in Fig. 4. We empirically set the trade-off parameter σ such as $\frac{1}{\sigma^2} = 0.001$ for all patients. We chose Cauchy–Navier

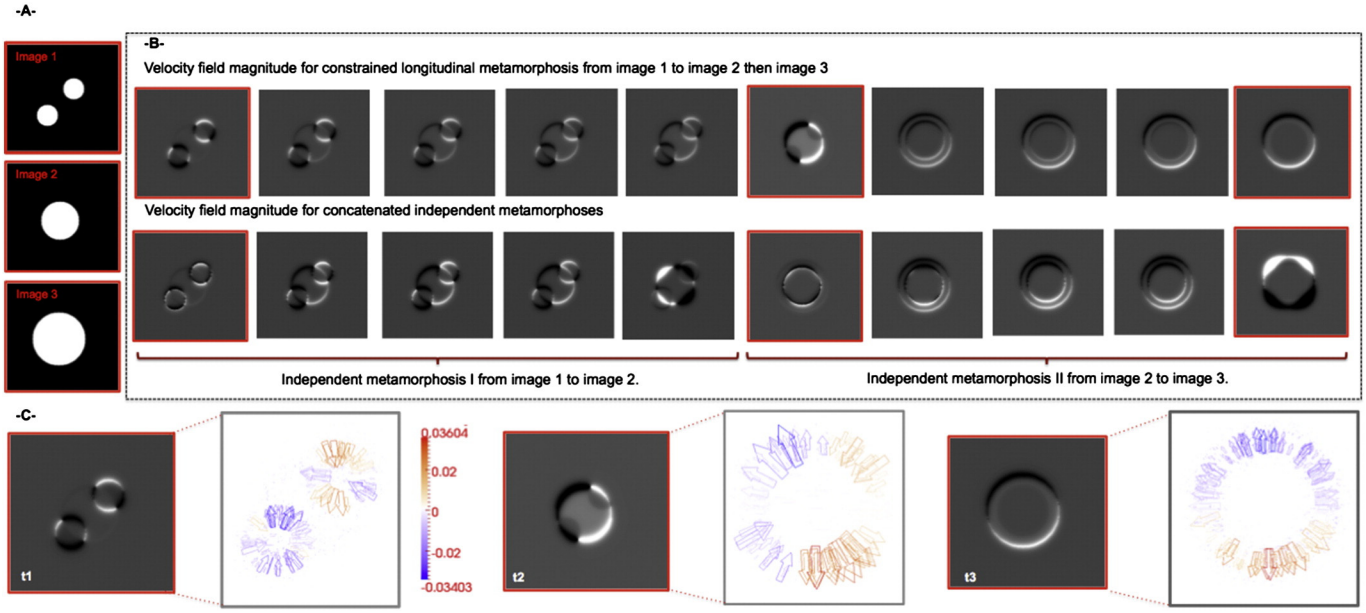

Fig. 3. Comparison between the proposed constrained longitudinal metamorphosis and independent metamorphoses using the estimated velocity field. (A) Synthetic data composed of three images. (B) (First row) We display successive snapshots of the estimated velocity magnitude map for the constrained longitudinal metamorphosis going through image 1, then image 2 and finally image 3. The velocity maps at the observation timepoints are highlighted in red. (Second row) We visualize the estimated velocity magnitude map for an image-to-image metamorphosis concatenating two independent metamorphoses: a first one from image 1 to image 2 and a second one from image 2 to image 3. (C) We visualize the velocity vector field on the x–y plane and its magnitude map at the observation timepoints. The color bar codes the velocity magnitude: the orange color represents positive magnitude (corresponding with bright areas in the gray-scale velocity magnitude maps) and the purple color represents negative magnitude (corresponding with dark areas in the gray-scale velocity magnitude maps).

differential operator L to provide greater smoothing of our data, justified in our study since we focus on obtaining a quantified estimate of the dynamics of ischemic lesion spatial margins. We set $\alpha = 0.01$ and $\gamma = 0.001$ as suggested by Beg et al. (2005).

We used the proposed longitudinal metamorphosis to exhibit and examine a single map (here residual map) generated for every patient. A significant property of the estimated residual map is that it condenses in one image both the magnitude of the deformation and the intensity variation in the lesion during its metamorphosis (see Fig. 5), thereby giving insights into the kinetic and photometric dynamic behavior of the perfusion lesion. We would also like to highlight that both residual and deformation maps were generated using the estimated in-between-observations I_t and v_t evolution paths while excluding the observation timepoints (our fixed boundaries) since the lesion evolution in space and time is mainly defined by these in-between estimated paths.

For each patient, we reconstruct the normalized residual map (rMap) as:

$$\text{For } x \in \Omega,\ \text{rMap}(x) = \sum_{t=0}^{T-1} \left| \Gamma\left(I_{t+1}\right)(x + v_t(x)) - I_t(x) \right|_{L^2}^2. \tag{9}$$

Then we normalize it between 0 and 1. The estimated residual maps quantify the variation in perfusion values inside the lesion under the action of the estimated deformation field. Therefore, residual areas with highest values mark where the most relevant dynamic change in both

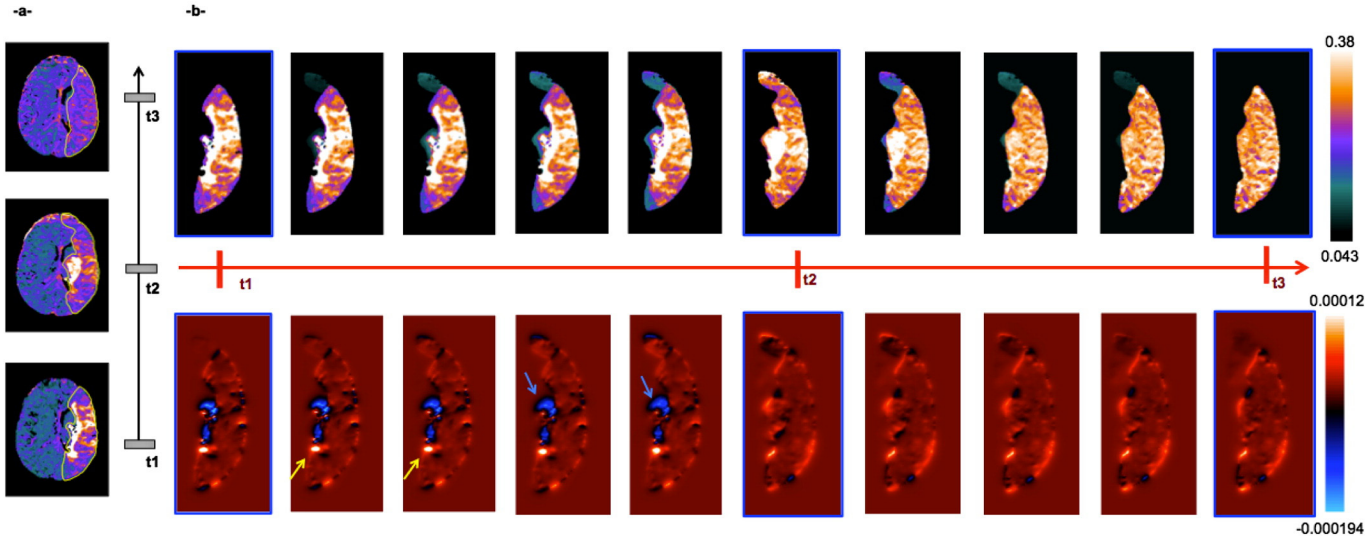

Fig. 4. Longitudinal metamorphosis. (a) MTT maps at three acquisition timepoints superimposed with the manual segmentation of the lesion (in yellow). (b) Top row: screenshots of the estimated intensity path ($t \mapsto I_t$) from t_1 to t_3 of MTT lesion metamorphosis; bottom row: screenshots of the estimated velocity path ($t \mapsto v_t$) from t_1 to t_3. Yellow arrows point to contracting areas and blue arrows point to expanding areas. Both of the displayed intensity and velocity maps are normalized (without a unit).

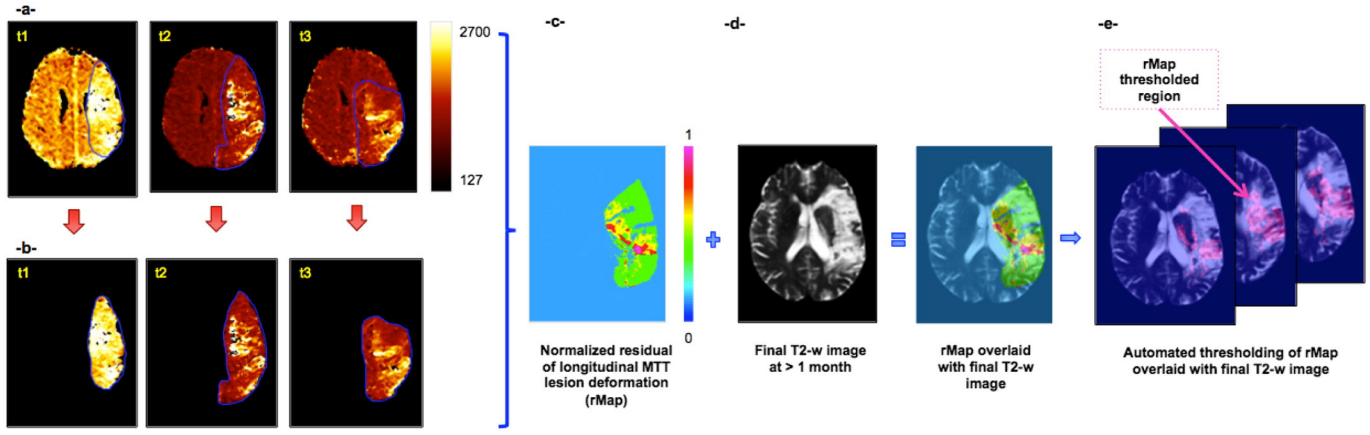

Fig. 5. Algorithm pipeline. (a) Three MTT images at three successive acquisition timepoints. (b) Extraction of the manually segmented MTT lesions (observations) that will be used in the longitudinal metamorphosis estimation. (c) Reconstruction of the metamorphosis-derived normalized residual map (rMap). (d) Overlaying the residual map with the final T2-w image. (e) Automatically thresholding the residual map and detecting the areas of highest change (in pink) — superimposed with final T2-w image.

intensity and shape takes place. To detect these areas with highest MTT variation from t_1 to t_3, we define an automated threshold as the mean value of rMap. Then, we generate a new normalized thresholded rMap by including all the voxels with values above this threshold. Fig. 5 visualizes the steps of the algorithm for every patient in our cohort. Finally, we compute the volumetric overlap (in %) between the thresholded residual map and T2-w lesion w.r.t. *final T2-w volume*. This volumetric overlap indicates how much of the final T2-w lesion is occupied by the thresholded residual map.

Using Eq. (9), the residual map includes the most relevant lesion changes in shape and intensity from t_1, to t_2 then to t_3; however, it does not inform us about the direction in which the perfusion change is going (positive direction i.e., increasing values or negative direction i.e., decreasing values). To interpret the thresholded rMap with regard to the direction of perfusion value variation — while only focusing on the acute and late perfusion changes, we generated a signed MTT map defined as the difference image between MTT image at t_3 and MTT image at t_1:

$$\text{For } x \in \Omega,\ \text{map}_{\Delta_{\text{MTT}}}(x) = \text{MTT}_{t_3}(x) - \text{MTT}_{t_1}(x).$$

Then, we mark areas in the thresholded residual map with negative (blue) and positive (red) $\text{map}_{\Delta\text{MTT}}$ values. This generates a signed thresholded residual map (Fig. 6) that allows us to simultaneously look at perfusion areas that underwent the highest intensity and deformation changes with distinction of areas where MTT values decreased from t_1 to t_3 (negative $\text{map}_{\Delta\text{MTT}}$ values) or increased from t_1 to t_3 (positive $\text{map}_{\Delta\text{MTT}}$ values). Positive regions in the signed $\text{rMap}_{\text{thresholded}}$ represent 'extreme' areas where the perfusion abnormality has worsened. In the other hand, negative regions highlight areas where the blood flow bettered.

4.3. Remark

The signed thresholded residual maps do not exceed the boundaries of the manual outlines of MTT lesions at the three acquisition timepoints. We also would like to point out that one could use Eq. (9) without the L^2 norm to generate the thresholded residual map. However, we preferred to restrict our analysis on only immediate change from acute (at t_1) to final (at t_3) dead tissue and not to consider the intermediate change that is governed by many unknown variables and pathophysiological

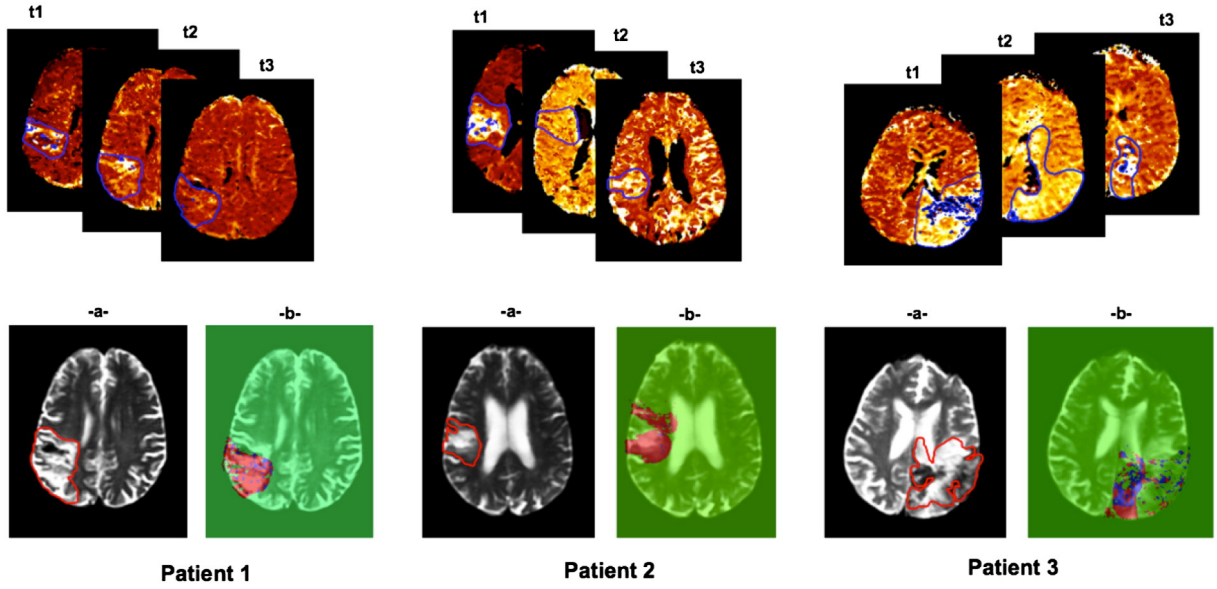

Fig. 6. Signed thresholded residual maps in three representative patients. Top row: same axial slices of one MTT lesion (outlined in blue) at three successive acquisition timepoints for three patients. Bottom row: (a) the final T2-w image where the final dead tissue is manually outlined in red. (b) Signed thresholded residual map (red color for positive values and blue color for negative values) overlaid with final T2-w image. Both images (a) and (b) represent the same axial slice.

'laws'. Comparing only the first to final tissue states is a common clinical assessment routine. We used it to shed light on the thresholded residual map.

4.4. Exploring the predictive potential of MTT maps using metamorphic residual maps

There exists a wide variation between patients in the total volumetric overlap between the thresholded metamorphic residual map and final T2-w lesion between patients (mean = 45.4%, standard deviation = 28% median = 32.8%). Positive skewness (Fig. 7-box 1) suggests that most patients deviate from the median with a wider range of volumetric overlap. This shows that the thresholded residual map marking abnormal perfusion areas with highest change in shape and intensity identifies relatively large dead areas within the T2-w lesion.

The most dynamic part of PWI lesion where perfusion was improving (i.e., negatively signed thresholded residual map) overlapped with the final T2 volume with range from 0 to 67%, mean = 26.1%, standard deviation = 19.3%, and median = 17.1% in our cohort. This shows that the acute–subacute improvement of the hemodynamics of the abnormal perfusion area does not necessarily imply that it will certainly end up outside the final T2-lesion. The negative overlap was evenly split at the median of the data (i.e., zero skewness, Fig. 7-box 2). Only Figs. 7-box 2 and 6 show that the majority of areas in the $rMap_{thresholded}$ are positively signed (red areas in Fig. 6), i.e., with worsened blood flow. This indicates that the thresholded residual map contains areas whose MTT values increased from t_1 to t_3, thus, identifying areas that are more likely to shift into an irreversible state of tissue death.

5. Discussion and conclusions

In the present work, we proposed a trivial extension of the work of Trouvé and Younes (2005) and Garcin and Younes (2005) for the image-to-image metamorphosis theory into a constrained longitudinal metamorphosis that passes exactly through the true observations, while forcing the geometric evolution to be continuous in time. We applied it to serial perfusion image data obtained in the acute to subacute stages in patients with ischemic stroke. This provided a robust, sophisticated mathematical tool to extract both dynamic and intensity features from the perfusion lesion summarized in the intensity variation and shape deformation residual map. We then used a static T2-w image at ≥1 month after stroke to determine the reversibility of the metamorphic residual of the perfusion lesion. We aimed to provide a sophisticated method, that is blind to clinical features (e.g., site of occlusion and stroke severity score), for evaluating the effect of variations in cerebral perfusion on tissue outcome. We hypothesized that the hypoperfused areas that underwent the most shape and intensity variation a) would have been exposed to the largest differences in perfusion values and b) the values would be consistent between tissues that behaved similarly.

We demonstrated that the estimation of longitudinal metamorphic residual maps is a promising tool in tracking the spatiotemporal changes in lesion shape and intensity. This overcomes major limitations of the commonly used 2D or 3D voxel-based or volume-subtraction methods that do not allow the estimation of dynamic characteristics of lesion progression or regression (Beaulieu et al., 1999; Karonen et al., 2000; Kluytmans et al., 2000; Rekik et al., 2012; Wittsack, 2002). Our model is fully automated and does not require any manual landmark matching. It is also generic so it could be applied to other medical applications based on serial imaging.

Using the automatically thresholded residual map, we showed that the amount of variation in MTT lesion shape and intensity identified a large portion of tissue that is irreversibility damaged. Thus, the MTT map showed promise for identifying dead tissue margins and tissue that survived, although there was substantial variation in the individual perfusion values. This means that it is difficult to identify any one MTT value that differentiates tissue destined to die from tissue that will survive between patients, as it is the dynamic properties of the MTT lesion that seem to determine tissue fate. The present model could be used to tailor more sophisticated models to predict tissue fate using the estimated evolution of the perfusion lesion shape and intensity. It could also be used to examine other factors that may influence ischemic lesion outcome such as blood pressure or pharmacological treatment. The signed residual maps showed that most of the abnormal perfusion tissue in which MTT values increased (with positive $map_{\Delta_{MTT}}$ values i.e., worsening of blood flow) belonged to the final T2-w boundary. However, some portions (negative overlap: mean = 26.1%, standard deviation = 19.3%) of the acutely ischemic tissue whose MTT values decreased (i.e., better blood flow) also ended up as dead tissue. This

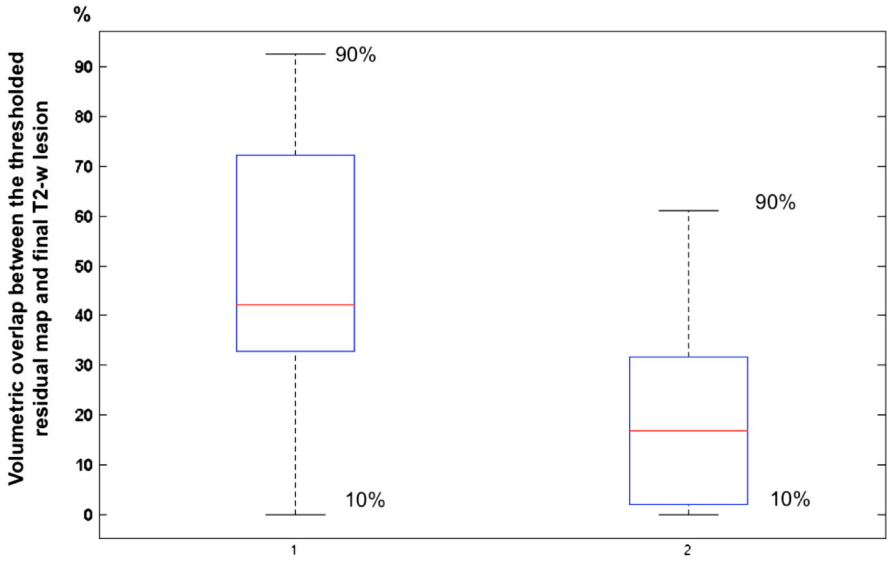

Fig. 7. Boxplot illustrating the skewness in our cohort for the volumetric overlap between thresholded metamorphic residual map ($rMap_{thresholded}$) and final T2-w lesion (box 1). Box 2 shows the distribution of the volumetric overlap between negatively signed $rMap_{thresholded}$ and final T2-w lesion. The red line represents the median value of the volumetric overlap. The lower boundary of the blue box represents the 25th percentile and the upper boundary represents the 75th percentile. The upper (vs. lower) horizontal line denotes the 90th (vs. the 10th) percentile.

highlights the potential for the most active positive residuals to be used in further predictive models to identify the boundaries of the final dead tissue.

One of the key clinical findings of our approach revealed the absence of a single threshold for rMap that fitted all patients. Patient-specific thresholds were automatically defined using the metamorphic residual maps. These thresholds involved both variation in MTT perfusion values and lesion shape change as the lesion evolved $[t_1, t_3]$ — showing that the evolution of ischemic but still viable tissue is patient-specific (and not dataset-specific). This is consistent with a recent summary (Dani et al., 2012) which did not identify a specific threshold or range of perfusion values that clearly discriminated tissue fate. Our method may have allowed us to capture some of the highly dynamic nature of perfusion values in individual parts of ischemic lesions for the first time in humans, as for example, have been shown in experimental models due to spreading depolarizations (Strong et al., 2007).

Several longitudinal studies have previously evaluated lesion evolution using standard thresholding and volumetric analysis techniques (Beaulieu et al., 1999; Karonen et al., 2000) to assess the combined role of perfusion or diffusion lesion in determining the degree of tissue survival or death. However, they did not explore the dynamic characteristics of lesion boundary evolution and their relation to its hemodynamics. A recent study (Carrera et al., 2011) noted that MTT perfusion values – outside and also within the DWI lesion – could be used to improve the identification of final infarct boundary. Two different perfusion thresholds were distinctively identified for two different datasets. Interestingly, in our study, we showed that perfusion values and spatiotemporal changes from acute to later stages are patient-specific and not dataset-specific, thereby demonstrating that perfusion thresholds or thresholds that depend on perfusion values are specific to each patient and not to a particular dataset. This accumulating evidence mitigates against the likelihood of finding universal and consistent perfusion values that identify at risk of infarction, dead and oligemic tissue in all patients and is expected to change the course of future clinical trials and patient selection criteria towards individualized medicine.

Identifying the shift in tissue abnormality, from being 'reversible' to being 'irreversible' in both space and time, is still one of the main challenges in stroke. The emergence of methods for dynamic modeling in stroke research shows potential for advancing our understanding of ischemic tissue dynamics. The key to a nuanced understanding of how perfusion values influence the spatial extent of tissue that will ultimately die or survive lies in refining the perfusion hypothesis (Butcher et al., 2005). This hypothesis states that abnormal perfusion areas where blood flow improved between acute and subacute stages will recover and those where blood flow worsened have the greatest likelihood to be irreversible. However, while this may be generally true, we have noticed in our study that there is substantial variation in perfusion values in space and time that limits use of specific perfusion values in prediction of tissue fate. Exposing the 'laws' that govern the hemodynamics of stroke would revolutionize stroke research. This may be achievable by using a more sophisticated version of longitudinal metamorphosis (e.g., by including tissue heterogeneity or other perfusion parameters or site of occlusion) that we have demonstrated which is now feasible.

Our study has some limitations. We did not account for differences in perfusion values between gray and white matter as ischemic lesions are difficult to segment into gray and white matter at present (Koga et al., 2005). We checked visually that the included patients did not have large amounts of lesion swelling as this could bias assessment of the final dead tissue volume. Accounting for acute swelling and late ex vacuo effect using more sophisticated registration algorithms would increase the accuracy of our method but validated techniques are not currently available. Our sample size was small — we chose these 10 patients to represent a range of lesion morphologies and changes over time to illustrate that the method was feasible and determine its potential for displaying dynamic stroke lesion pathophysiology. It was not our intention to provide definitive perfusion values or to examine how, for example perfusion values might influence diffusion values, or the impact of clinical variables. This is subject to future work in larger datasets with a more personalized version of the implemented metamorphosis method.

6. Conclusion

We used longitudinal metamorphosis to track the evolution of perfusion abnormality in stroke using time-series imaging. This model provides novel ways to identify the most active changes in ischemic lesion hemodynamics using signed residual maps and we believe will be valuable in future stroke research to clarify what determines ischemic lesion evolution and identify new potential targets for development of new treatments to increase the change of better clinical recovery. The application of the metamorphosis model to scattered and solitary perfusion stroke lesions has led us to a set of observations: some are partly consistent with stroke literature such as the role that perfusion values play in determining final tissue fate, and others pave the way for a paradigm shift with regard to the 'universality' of perfusion values in determining final tissue fate. We have also presented a novel powerful analysis tool (metamorphic residual map) for extracting both kinetic and intensity features from time-series imaging. Future work includes integrating new clinical variables into the longitudinal metamorphosis model and validating our findings in larger datasets using different perfusion maps. Moreover, this model and algorithm are not specific to stroke lesions and could be used to model other brain diseases' evolution with topology change such as hematoma or white matter hyperintensities or tumors.

References

Allassonnière, S., Trouvé, A., Younes, L., 2005. Geodesic shooting and diffeomorphic matching via textured meshes. EMMCVPR, pp. 365–381.

Bastin, M., Armitage, P., 2000. On the use of water phantom images to calibrate and correct eddy current induced artefacts in MR diffusion tensor imaging. Magn. Reson. Imaging 18, 681–687.

Beaulieu, C., Crespigny, A.D., Tong, D., Moseley, M., Albers, G., Marks, M., 1999. Longitudinal magnetic resonance imaging study of perfusion and diffusion in stroke: evolution of lesion volume and correlation with clinical outcome. Ann. Neurol. 46, 568–578.

Beg, M., Miller, M., Trouvé, A., Younes, L., 2005. Computing large deformation metric mappings via geodesic flows of diffeomorphisms. Int. J. Comput. Vis. 61, 139–157.

Butcher, K., Parsons, M., Macgregor, L., Barber, P., Chalk, J., Bladin, C., Levi, C., Kimber, T., Schultz, D., Fink, J., 2005. Refining the perfusion–diffusion mismatch hypothesis. Stroke 36, 1153–1159.

Carrera, E., Jones, P., Alawneh, J., Mikkelsen, I., Cho, T., Siemonsen, S., Guadagno, J., Mouridsen, K., Hjort, L.R., 2011. Predicting infarction within the diffusion-weighted imaging lesion: does the mean transit time have added value? Stroke 42, 1602–1607.

Dani, K.A., Thomas, R.G.R., Chappell, F.M., Shuler, K., Muir, K.W., Wardlaw, J.M., 2012. Systematic review of perfusion imaging with computed tomography and magnetic resonance in acute ischemic stroke: heterogeneity of acquisition and postprocessing parameters: a translational medicine research collaboration multicentre acute stroke imaging study. Stroke 43, 563–566.

Davis, S., Donnan, G., Parsons, M., Levi, C., Butcher, K., Peeters, A., Barber, P., Bladin, C., Silva, D.D., Byrnes, G., 2008. Effects of alteplase beyond 3 h after stroke in the Echoplanar Imaging Thrombolytic Evaluation Trial (EPITHET): a placebo-controlled randomised trial. Lancet Neurol. 7, 299–309.

Dupuis, P., Grenander, U., Miller, M., 1998. Variational problems on flows of diffeomorphisms for image matching. Q. Appl. Math. 56, 587.

Furlan, A., Eyding, D., Albers, G., Al-Rawi, Y., Lees, K., Rowley, H., Sachara, C., Soehngen, M., Warach, S., Hacke, W., 2006. Dose Escalation of Desmoteplase for Acute Ischemic Stroke (DEDAS): evidence of safety and efficacy 3 to 9 hours after stroke onset. Stroke 37, 1227–1231.

Garcin, L., Younes, L., 2005. Geodesic Image Matching: A Wavelet Based Energy Minimization Scheme. pp. 349–364.

Hacke, W., Albers, G., Al-Rawi, Y., Bogousslavsky, J., Davalos, A., Eliasziw, M., Fischer, M., Furlan, A., Kaste, M., Lees, K., 2005. The Desmoteplase in Acute Ischemic Stroke Trial (DIAS): a phase II MRI-based 9-hour window acute stroke thrombolysis trial with intravenous desmoteplase. Stroke 36, 66–73.

Holland, D., Dale, A., 2011. Nonlinear registration of longitudinal images and measurement of change in regions of interest. Med. Image Anal. 15, 489–497.

Hong, Y., Joshi, S., Sanchez, M., Styner, M., Niethammer, M., 2012. Metamorphic geodesic regression. Medical Image Computing and Computer-Assisted Intervention — MICCAI 2012, pp. 197–205.

Huang, H., Ceritoglu, C., Li, X., Qiu, A., Miller, M., Zijl, P.V., Mori, S., 2008. Correction of B0 susceptibility induced distortion in diffusion-weighted images using large-deformation diffeomorphic metric mapping. Magn. Reson. Imaging 26, 1294–1302.

Karonen, J., Liu, Y., Vanninen, R., Ã˜stergaard, L., Partanen, P., Vainio, P., Vanninen, E., Nuutinen, J., Roivainen, R., Soimakallio, S., 2000. Combined perfusion- and diffusion-weighted MR imaging in acute ischemic stroke during the 1st week: a longitudinal study[1]. Radiology 217, 886–894.

Klein, A., Andersson, J., Ardekani, B., Ashburner, J., Avants, B., Chiang, M., Christensen, G., Collins, D., Gee, J., Hellier, P., 2009. Evaluation of 14 nonlinear deformation algorithms applied to human brain MRI registration. NeuroImage 46, 786–802.

Kluytmans, M., Everdingen, K.V., Kappelle, L., Ramos, L., Viergever, M., Grond, J.V.D., 2000. Prognostic value of perfusion- and diffusion-weighted MR imaging in first 3 days of stroke. Eur. Radiol. 10, 1434–1441.

Koga, M., Reutens, D., Wright, P., Phan, T., Markus, R., Pedreira, B., Fitt, G., Lim, I., Donnan, G., 2005. The existence and evolution of diffusion–perfusion mismatched tissue in white and gray matter after acute stroke. Stroke 36, 2132–2137.

Niethammer, M., Huang, Y., Vialard, F.X., 2011. Geodesic Regression for Image Time-Series. pp. 655–662.

Ogata, T., Nagakane, Y., Christensen, S., Ma, H., Campbell, B., Churilov, L., Olivot, J., Desmond, P., Albers, G., Davis, S., 2011. A topographic study of the evolution of the MR DWI/PWI mismatch pattern and its clinical impact: a study by the EPITHET and DEFUSE investigators. Stroke 42, 1596–1601.

Rekik, I., Allassonnière, S., Carpenter, T., Wardlaw, J., 2012. Medical image analysis methods in MR/CT-imaged acute–subacute ischemic stroke lesion: segmentation, prediction and insights into dynamic evolution simulation models. A critical appraisal. NeuroImage Clin. 1 (1), 164–178.

Rekik, I., Allassonnière, S., Durrleman, S., Carpenter, T., Wardlaw, J., 2013. Spatiotemporal dynamic simulation of acute perfusion/diffusion ischemic stroke lesions evolution: a pilot study derived from longitudinal MR patient data. Computational and Mathematical Methods in Medicine 2013.

Rivers, C.S., Wardlaw, J.M., Armitage, P.A., Bastin, M.E., Hand, P.J., Dennis, M.S., 2007. Acute ischemic stroke lesion measurement on diffusion-weighted imaging — important considerations in designing acute stroke trials with magnetic resonance imaging. J. Stroke Cerebrovasc. Dis. 16, 64–70.

Strong, A., Anderson, P., Watts, H., Virley, D., Lloyd, A., Irving, E., Nagafuji, T., Ninomiya, M., Dunn, H.N., 2007. Peri-infarct depolarizations lead to loss of perfusion in ischaemic gyrencephalic cerebral cortex. Brain 130, 995–1008.

Trouvé, A., 1995. An Approach of Pattern Recognition Through Infinite Dimensional Group Action.

Trouvé, A., 1998. Diffeomorphisms groups and pattern matching in image analysis. Int. J. Comput. Vis. 28, 213–221.

Trouvé, A., Younes, L., 2005. Metamorphoses through lie group action. Found. Comput. Math. 5, 173–198.

Wardlaw, J., 2010. Neuroimaging in acute ischaemic stroke: insights into unanswered questions of pathophysiology. J. Intern. Med. 267, 172–190.

Wardlaw, J., Murray, V., Berge, E., Zoppo, G.D., Sandercock, P., Lindley, R., Cohen, G., 2012. Recombinant tissue plasminogen activator for acute ischaemic stroke: an updated systematic review and meta-analysis. Lancet 379, 2364–2372.

Wittsack, H., 2002. MR Imaging in Acute Stroke: Diffusion-weighted and Perfusion Imaging Parameters for Predicting Infarct Size[1].